



Characterisation of fatigue damage in asphalt mixtures using X-ray computed tomography

Anqi Chen, Gordon D. Airey, Nick Thom & Yuanyuan Li

To cite this article: Anqi Chen, Gordon D. Airey, Nick Thom & Yuanyuan Li (2022): Characterisation of fatigue damage in asphalt mixtures using X-ray computed tomography, Road Materials and Pavement Design, DOI: [10.1080/14680629.2022.2029756](https://doi.org/10.1080/14680629.2022.2029756)

To link to this article: <https://doi.org/10.1080/14680629.2022.2029756>



© 2022 The Author(s). Published by Informa UK Limited, trading as Taylor & Francis Group



Published online: 02 Feb 2022.



Submit your article to this journal [↗](#)



Article views: 47




View related articles [↗](#)



View Crossmark data [↗](#)

Characterisation of fatigue damage in asphalt mixtures using X-ray computed tomography

Anqi Chen ^a, Gordon D. Airey^a, Nick Thom^a and Yuanyuan Li^b

^aFaculty of Civil Engineering, Nottingham Transportation Engineering Centre, University of Nottingham, Nottingham, UK; ^bSchool of Civil Engineering and Architecture, Wuhan Institute of Technology, Wuhan, People's Republic of China

ABSTRACT

The high-resolution X-ray CT was applied to investigate the fatigue damage evolution of asphalt mixtures. The detailed X-ray CT images in the centre of the samples were used to characterise the fatigue cracking and air voids increase at different vertical deformations. Air void content and surface area distribution before and after loading were also analysed. The results show that the main failure mode of asphalt mixtures at low temperature is debonding at the interface between aggregates and mastic, which is an adhesive failure. The maximum change of air void content due to fatigue damage often occurs near the middle of the sample. Cracks were observed in and around flat and elongated aggregates and on aggregates with insufficient fracture faces, demonstrating the effects of aggregate angularity and shape on fatigue cracking. The microcracks develop continuously throughout the entire fatigue process.

ARTICLE HISTORY

Received 30 March 2021
Accepted 11 January 2022

KEYWORDS

Asphalt mixtures; X-ray computed tomography; microstructure; fatigue damage; indirect tensile fatigue test

1. Introduction

Asphalt concrete is the most commonly used construction material in pavements throughout the world and its internal structure has been the focus of various research studies (Monismith, 1992). The anisotropy of the microstructure causes complex mechanical responses to variables such as temperature and loading, which in turn influences the performance of asphalt concrete (Eriksen, 1993). Visualising the internal structure is critical in determining microstructural damage mechanisms and relating to the performance of asphalt concrete. Nonetheless, traditional laboratory and field tests generally do not allow visualisation of the internal structure of an asphalt mixture. Digital imaging techniques have been proposed as a solution to this issue and have been shown by a number of researchers (Masad et al., 1999; Tashman et al., 2000; Yue, et al., 1995) to be effective for evaluating the internal structure of asphalt concrete.

Over the last decade, there has been significant improvement in the capabilities of digital imaging techniques with technology development and advances in equipment availability (Masad et al., 2002). Tomographic images obtained from X-ray computed tomography (CT) have been used to successfully research the microstructure of asphalt concrete (Wang et al., 2004). The X-ray CT technique is able to visualise the damage evolution inside an asphalt mixture specimen as well as the internal structure of the materials in three-dimensions (3D) (Braz et al., 1999; Khan, 2010; Tashman et al., 2004). Further structural analysis including aggregate orientations, air voids content and air voids area distribution can be used to segment asphalt mixture composition from tomographic images through digital image

CONTACT Anqi Chen  anqi.chen@nottingham.ac.uk

processing (DIP). This can be done using techniques such as contrast enhancement, noise reduction, grey intensity thresholding and binarisation (Kutay, et al., 2010; Zelelew & Papagiannakis, 2011).

Recent literature has had two main focuses; firstly, showing the significant role of air voids and aggregate properties on the mechanical behaviour of asphalt pavements (Aliha et al., 2015; Castillo et al., 2015; Coleri et al., 2012, 2013; Khosravi et al., 2013; Kodippily et al., 2014; Mohajeri et al., 2014) and secondly, in developing 2D and 3D microstructure numerical models (Dai, 2010; Kim, et al., 2010; Liu et al., 2017; Rami et al., 2017; Trawiński et al., 2018; Zhang et al., 2006). However, few studies have applied X-ray CT for characterising fatigue damage (Seo & Kim, 2008; Tashman et al., 2005). In one such study, the damage was defined by Song using X-ray CT images which were scanned at 1 mm intervals (Song, 2004). X-ray CT was also used by Khan and Collop (2010) to quantify the damage induced during constant strain rate and fatigue tests. They concluded that the damage increased with increasing strain and there is a greater increase in damage (increased air voids content) for specimens tested at higher temperatures and lower strain rates. The disadvantage of X-ray CT is that it is difficult to obtain high-resolution images with large asphalt mixture samples. Detailed microcrack evolution is often not visible in low resolution and low resolution also results in inaccurate data as the thresholding might be affected.

This paper applied high-resolution X-ray CT (with a resolution of 0.014mm) to investigate the fatigue damage evolution of asphalt mixtures at the micro-level. To achieve this aim, samples (20 mm diameter and 18 mm height) were specially designed to visualise detailed fatigue crack geometry. All samples were tested using the indirect tensile fatigue test (ITFT) at 5°C and were set to stop at given vertical deformations of 0.4, 0.6, 0.8, 0.9, 1.1 and 1.4 mm, which represented distinct fatigue damage stages. The detailed X-ray CT images in the centre of the samples were used to characterise the fatigue cracking and air voids increase at different vertical deformations. By analysing air void content and surface area distributions before and after loading, it is possible to investigate damage evolution in different directions at different vertical deformations. The X-ray CT images of samples, where the maximum change of air voids content occurs were used to investigate the effect of the aggregate size and the distance between aggregates on fatigue damage.

2. Experimental methods

2.1. Materials

A 40/60 penetration grade bitumen was used, and the technical parameters of which are shown in Table 1. Aggregates used in this paper are granite collected from Bardon Hill quarry, Leicestershire, UK. Asphalt mixtures with nominal maximum aggregate size (NMAs) of 14 mm were chosen. Bitumen content was maintained at 5% by the weight of the mixture. The design gradation curve of the 14 mm Dense Bitumen Macadam (DBM), a UK-specified form of asphalt concrete, is shown in Figure 1 (British Standards Institution, 2016a). Asphalt mixtures were compacted by a roller compactor; mixing and compaction procedures of the asphalt mixtures were chosen from BS EN 12697-35: 2016 (British Standards Institution, 2016b) and BS EN 12697-33: 2019 (British Standards Institution, 2019).

Table 1. Properties of Pen 40/60 bitumen.

Properties	Binder	Test methods
Specific gravity	1.030	BS 2000-549:2007 (British Standards Institution, 2007)
Penetration (25°C, 5 s, 100 g)/0.1 mm	43	BS EN 1462:2015 (British Standards Institution, 2015a)
Softening point/°C	51.1	BS EN 1427:2015 (British Standards Institution, 2015b)
Viscosity, 135°C/mPa s	441.3	BS EN 13302:2018 (British Standards Institution, 2018a)

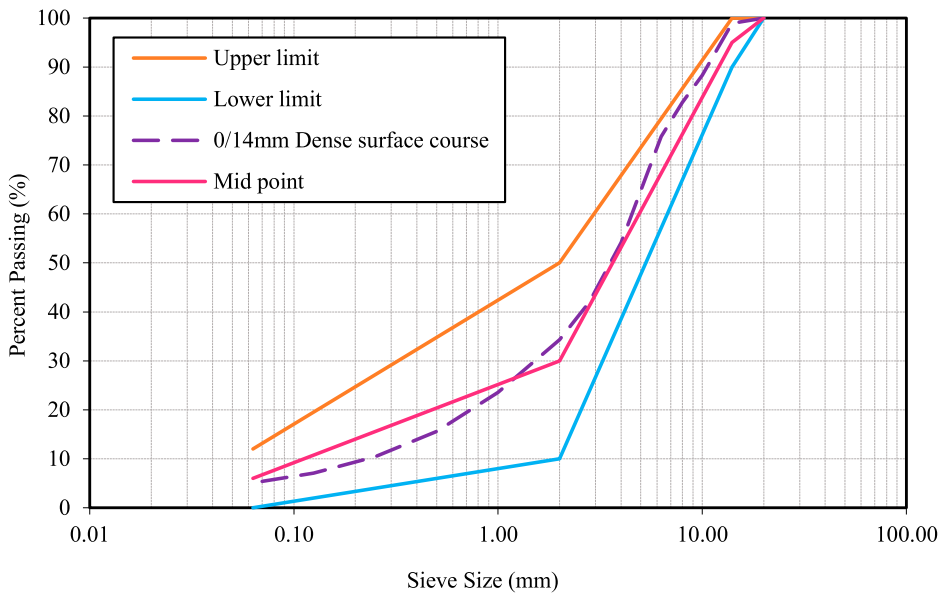


Figure 1. Gradation of 14 mm DBM asphalt mixture.

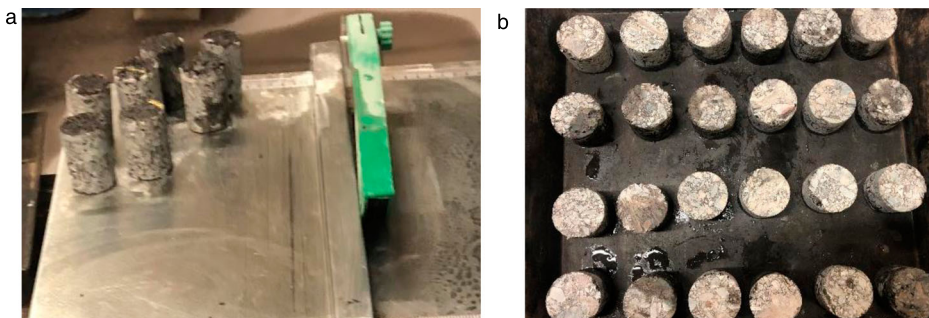


Figure 2. (a) Cutting procedure; (b) Prepared samples.

2.2. Indirect tensile fatigue test

Specimens of dimensions 20 mm diameter by 18 mm height were made for use in the ITFT equipment, and the cutting procedure and the prepared samples are shown in Figure 2. Small specimens were designed for the X-ray CT test because that X-ray radiation is absorbed differently passing through different depths, and standard specimens were found to absorb more X-ray radiation, leading to less X-ray radiation penetrating through and producing less clear images. The air voids content of small specimens was tested before ITFTs to make sure they are around 5%. Specimens with too low or too high air voids content will not be used for testing. Three trial specimens were tested; results show that three specimens failed when the vertical deformations were approximately 2 mm, and the number of cycles at failure were similar, proving that the special size specimen is also suitable for ITFTs.

Fatigue damage is caused by a combination of various factors, and this combined effect is more complicated at low temperatures. Based on our previous work, we found that there exists a worst-case temperature for fatigue life of asphalt concrete in the range of 5–10°C (Chen et al., 2021; Maggiore & Airey, 2014; Read et al., 1996). The specimens are too small that we want to reduce the effect of high-temperature deformation on specimens, so that we can observe more microcracks development.

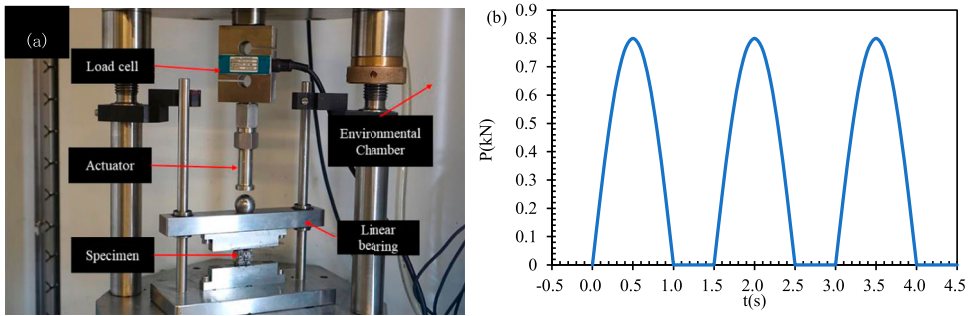


Figure 3. (a) Indirect tensile fatigue test set-up; (b) Schematic diagram of the load during the ITFT.

Therefore, the temperature of 5°C is chosen in this study. The specimens were conditioned at the test temperature, $5 \pm 1^{\circ}\text{C}$, and then positioned perpendicular, between the top and bottom loading strips (Figure 3(a)). Figure 3(b) illustrates a repeated controlled stress pulse applied at a rate of 40 pulses per minute at a load of 0.8 kN. The cumulative vertical deformation versus the number of load cycles was recorded. Tests stopped automatically when the vertical deformation exceeded the set values of 0.4, 0.6, 0.8, 0.9, 1.1 and 1.4 mm (British Standards Institution, 2018b). After the test, in order to avoid changes (i.e. crack healing) before CT scanning, all the specimens were stored at -5°C . As the specimen is not the standard size, the strain gauge was applied on the specimen with the 1.4 mm vertical deformation to record the strain level.

2.3. X-ray CT set-up

For the microstructure analysis, the specimens were X-rayed before and after the ITFT. The scanner consists of an X-ray tube, a rotation stage and a detector (Figure 4). The X-ray CT scanning was conducted under a penetration of 180 kV and a contrast of 80 mA with the resulting resolution is 0.014 mm. During scanning, the small sample (Figure 4(b)) is shifted vertically and the entire procedure is repeated to generate additional 2D image slices. The images were processed using the VGStudio Max software.

3. Image analysis methods

3.1. Digital image processing

Figure 5 illustrates the processing procedure used with the CT X-ray images. Figure 5(b) shows a typical 2D image from an asphalt mixture specimen, the brightest region (highest density) represents the aggregates, followed by the mastic (bitumen and filler) and the darkest regions represent air voids (lowest density). The 2D slices can be rendered to produce a 3D image as shown in Figure 5(h). In this study, digital image processing (DIP) is used to process X-ray CT images, including adjustments to improve the image quality, such as grey intensity thresholding and image segmentation. An image profile was generated to identify the range of possible threshold values in the Area of Interest (AOI). As shown in Figure 5(c), pixels (grey values) are shaded separately in different colours to group the ranges of grey values for the specified materials in the mixture. These grey values are used to identify those pixels that belong to the AOI for detecting the threshold values. Thresholding is carried out to isolate the AOI within an image from the background based on pixel intensity. Phase (aggregates, mastic and air voids) isolation was achieved by applying different threshold values, as shown in Figure 5(e–g). A pseudo colour was applied to the original image to view the material phases, by assigning each of them a different colour spectrum (Figure 5(d)).

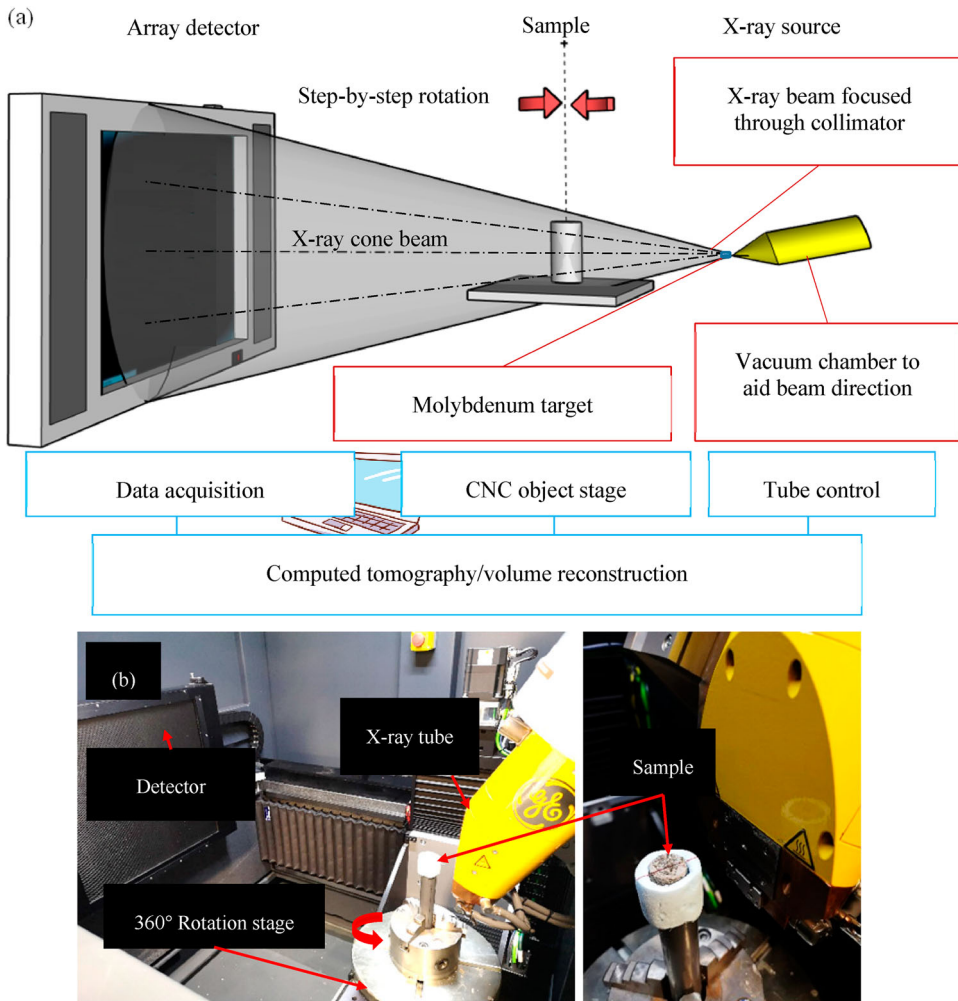


Figure 4. (a) Schematic of industrial X-ray CT system; (b) X-ray CT equipment set-up.

3.2. The coordinate axis and the image area for calculation

Six asphalt specimens were analysed at different vertical deformations to establish the air voids distribution, where the Y -axis is the loading direction and the X and Z axes are in the horizontal plane with the Z -axis in the direction of the specimen height. To make sure the calculated area is the same for each slice, the image area as shown in Figure 6 is applied for calculation.

3.3. Calculation equations of volume and surface area parameters

The volume and surface area parameters of air voids were calculated to determine the damage evolution and fatigue resistance properties of the sample. Total sample volume (SV , mm^3), air voids volume (AVV , mm^3) and air voids surface area ($AVSA$, mm^2) before and after loading were calculated by software VGStudio Max 3.0.0. Air voids content (AVC , %), air voids content change ($AVCC$, %) and air voids content increase ($AVCI$, %) were calculated using Equations 1–3. Surface area change ($AVSAC$, mm^2)

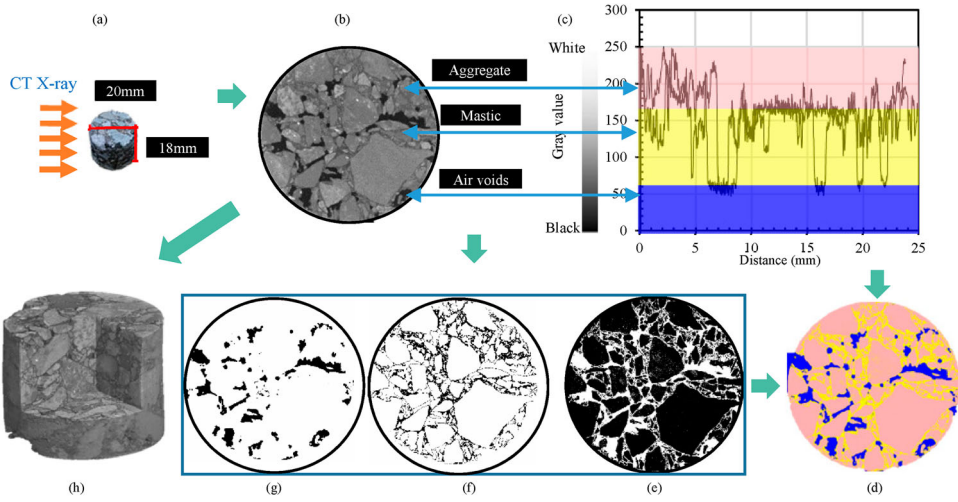


Figure 5. CT X-ray images processing; (a) the geometry and dimensions of samples; (b) central CT slice image; (c) AOI extracted by grey value; (d) after pseudo colour transformation; the phase (e) aggregates; (f) mastic and (g) air voids after adjusting the threshold values; (h) 3D reconstruction from 2D slices.

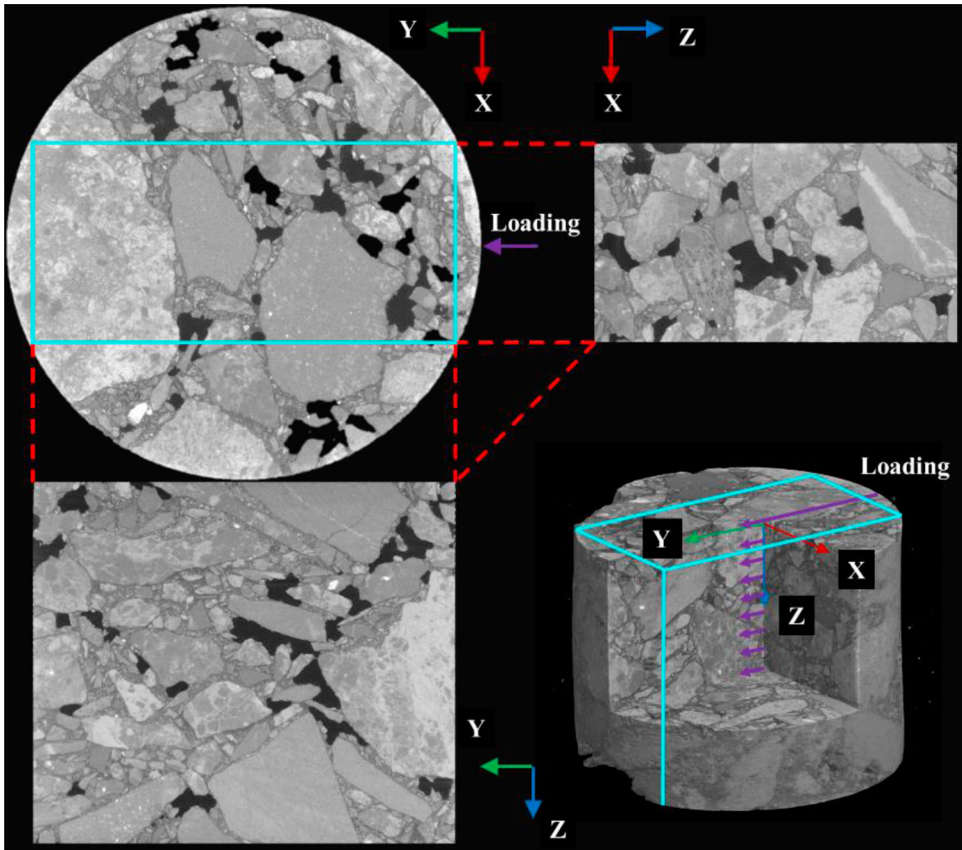


Figure 6. The coordinate axis and the image area for calculation.

and surface area increase (AVSAI, %) of air voids were calculated by Equations (4) and (5).

$$AVC = \frac{AVV}{SV} \times 100\% \quad (1)$$

$$AVCC = AVC_{\text{after}} - AVC_{\text{pre}} \quad (2)$$

$$AVCI = \frac{AVC_{\text{after}} - AVC_{\text{pre}}}{AVC_{\text{pre}}} \times 100\% \quad (3)$$

$$AVSAC = AVSA_{\text{after}} - AVSA_{\text{pre}} \quad (4)$$

$$AVSAI = \frac{AVSA_{\text{after}} - AVSA_{\text{pre}}}{AVSA_{\text{pre}}} \times 100\% \quad (5)$$

where AVC_{pre} , AVC_{after} , $AVSA_{\text{pre}}$ and $AVSA_{\text{after}}$ are air voids content and air voids surface area before and after loading.

4. Results and discussions

4.1. Fatigue damage evolution

To explore the damage evolution, the number of loading cycles vs. the vertical deformation was recorded as shown in Figure 7(a). It can be seen that there are three distinct stages which represent the different fatigue damage stages. In the first stage, deformation develops rapidly before slowing down. In the second stage, vertical deformation develops approximately linearly while finally in the third stage, the deformation becomes rapid once again.

Strain gauge with the full scale of $1 \mu\epsilon$ was glued in the centre of the sample during ITFTs to find the relationship between the vertical deformation and the strain level. In Figure 7(b), the strain vs. time curve changes from a smooth relationship to a significantly noisier relationship at the transition point (Time = 1578 s, Strain = 3960×10^{-6}), which is caused by cracks initiating near the strain gauge. The time (1578 s) corresponds to the vertical deformation 0.47 mm in Figure 7(c), and also to the first stage in Figure 7(a). The strain vs. time curve increases significantly at the point (Time = 4494 s, Strain = 13411×10^{-6}), for the reason that the strain gauge exceeds the full-scale value when cracks propagate quickly. The time (4494 s) corresponds to the vertical deformation 0.76 mm in Figure 7(c), and also to the second stage in Figure 7(a).

To explore how cracks initiate and propagate in each stage, images in the centre of the samples were captured. The main failure mode of asphalt at low temperatures is debonding at the surface between aggregates and mastic, which is an adhesive failure (Figure 8). Figure 8(a,b) corresponds to the first stage, where deformation is relatively small. A number of microcracks initiate at the aggregate–mastic interfaces. In fracture mechanics (Dowling, 1976; Jacobs et al., 1996; Majidzadeh et al., 1971; Paris, 1963; Sulaiman & Stock, 1995; Yin et al., 2015), the first stages are known as pre-cracking and transition. The process where stresses begin to accumulate in the sample to form microcracks is called pre-cracking and the process when micro-cracking begins to occur and propagate is called transition. Transition happens when the peak load of the sample occurs in the microcrack nucleation. Figure 8(c,d) corresponds to the second stage, where deformation increases linearly. Air voids expand in a small range and several microcracks connect together. This stage is defined as stable cracking. During this stage, microcracks propagate steadily causing the vertical deformation also to increase steadily. Figure 8(e,f) corresponds to the third stage, where air voids expand rapidly, and at the same time cracks develop quickly. This stage is defined as fully cracked. With the vertical deformation increasing rapidly, macrocracks initiate and propagate until the sample becomes fully damaged.

To present the change in the red area (the development of microcracks and air voids after loading) in Figure 8 clearly, the surface area of the red area is calculated by Equation (4) using ImageJ,

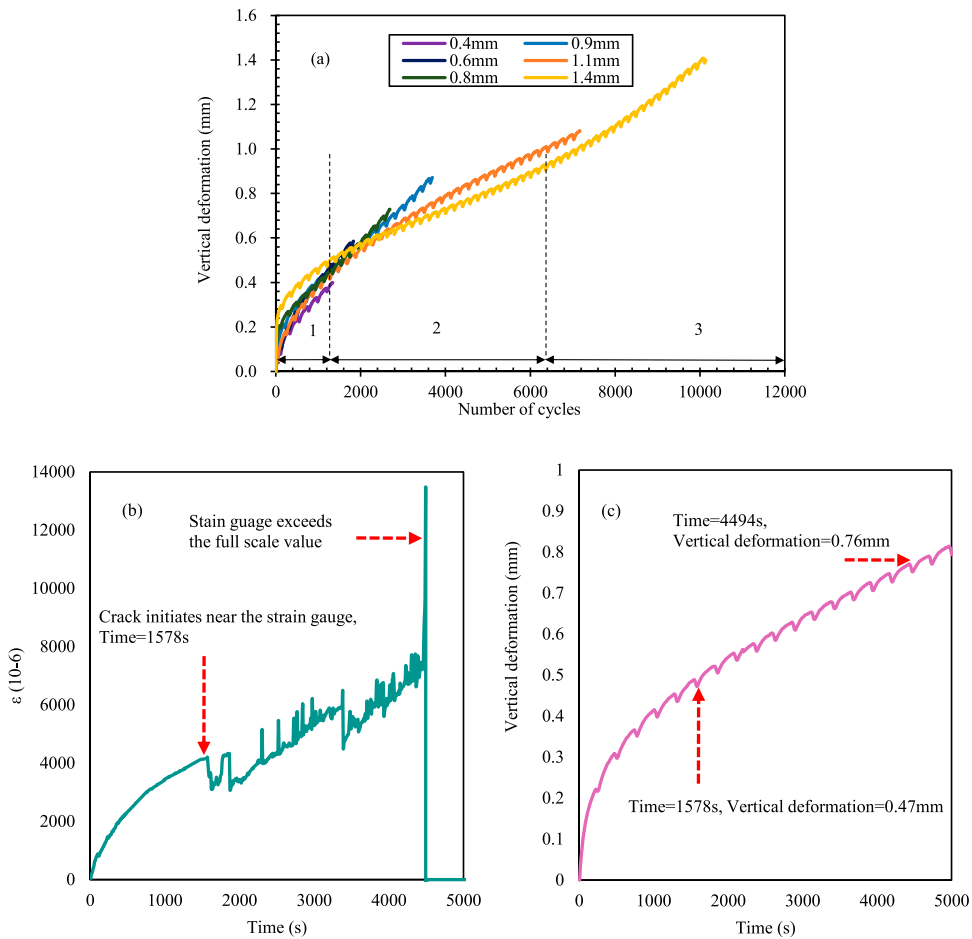


Figure 7. (a) Vertical deformation vs. number of cycles showing three different fatigue damage stages; (b) Strain vs. time curve; (c) Vertical deformation vs. time curve.

as shown in Figure 9. Seen from Figure 9, development of microcracks and air voids increases with the increase of the vertical deformation, and the development becomes faster after the deformation is 0.8 mm, while slower after 1.1 mm, which further defines that there exist three different evolution stages during fatigue damage process.

4.2. Air voids content distribution

The air voids content (AVC, %) distribution in the X and Y directions was calculated. The average AVC was calculated per 100 X-ray CT images (100 intervals). Due to the limitation of space, just three examples are shown in Figure 10. In the figure, the purple line represents the AVC before loading and the blue line is after vertical deformation. For the results calculated, for both the X and Y directions, the change of the AVC after loading becomes more obvious with the increase of vertical deformation. The change of the AVC can reflect the fatigue damage evolution.

Increase in the AVC in the Y direction was calculated. Two examples and the corresponding images at the position of the max and min increase in the AVC are shown in Figure 11. When vertical

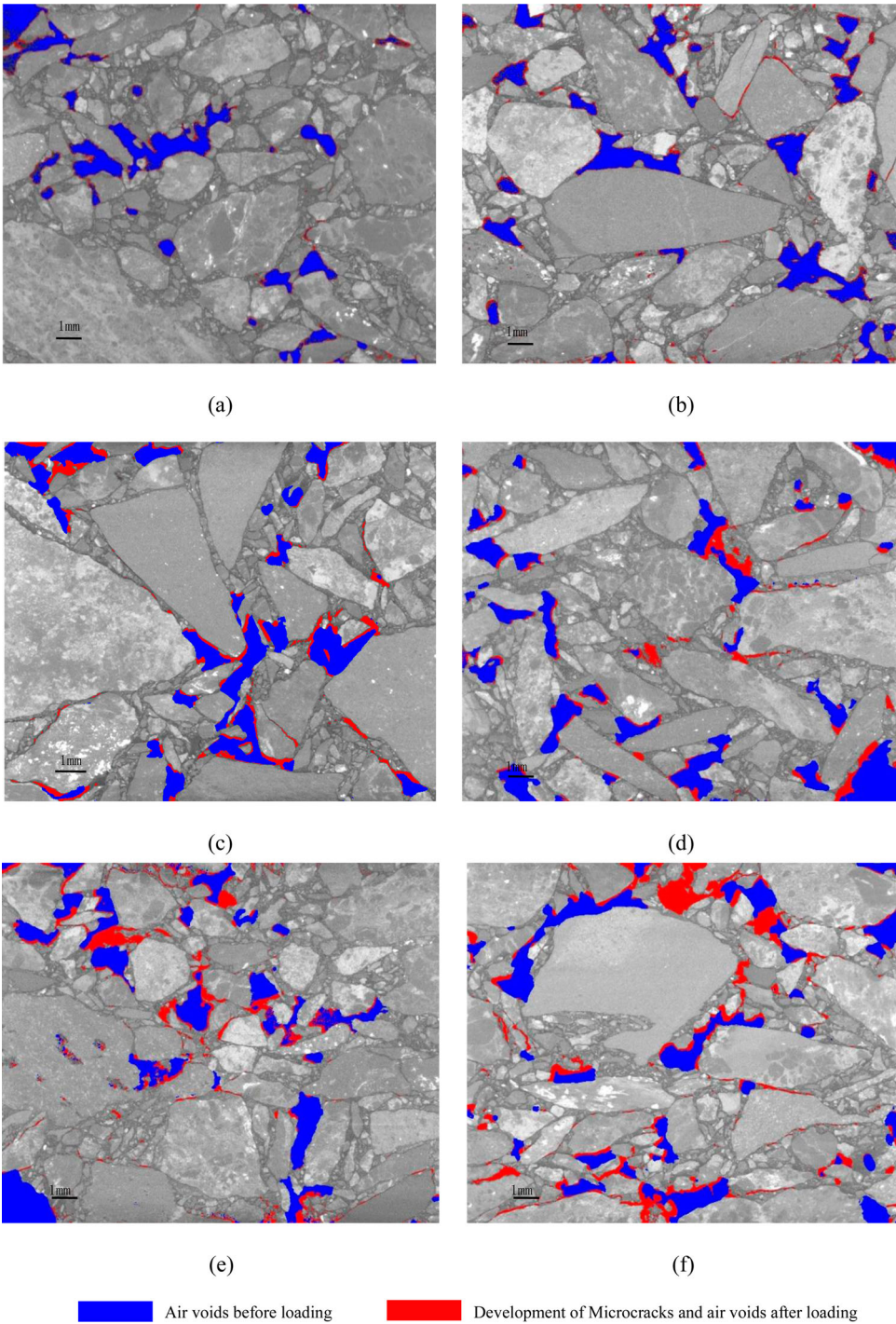


Figure 8. Air voids of unloaded samples and microcracks of loaded samples under different vertical deformation: (a) 0.4 mm; (b) 0.6 mm; (c) 0.8 mm; (d) 0.9 mm; (e) 1.1 mm and (f) 1.4 mm.

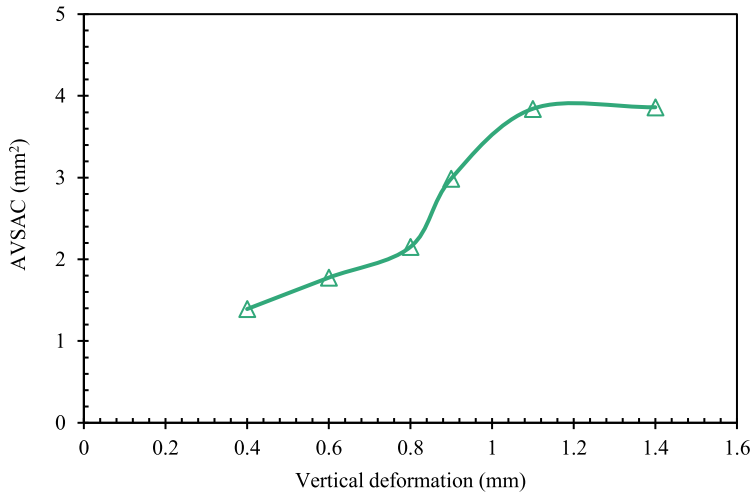


Figure 9. Air voids surfaces area change (AVSAC) versus vertical deformation.

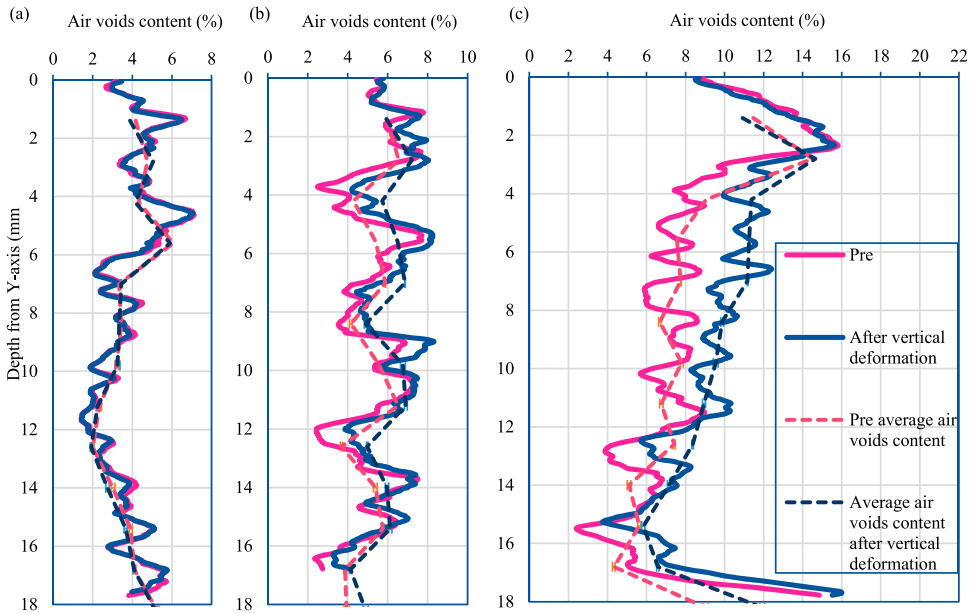


Figure 10. Air voids distribution in Y direction at (a) 0.4 mm; (b) 0.9 mm; (c) 1.4 mm vertical deformation.

deformation is 0.4 mm, the increase values in the AVC are mainly negative, and the max and min increase in the AVC occurred at the edge, proving that the specimen is in volumetric compression. When the vertical deformation is 0.6 mm, the increase values in the AVC are mainly positive. The max increase in the AVC occurred in the middle part of the sample, showing the specimen to be undergoing tensile strain (Miljković & Radenberg, 2014). Similar results were concluded for the other vertical deformations (0.8, 0.9, 1.1 and 1.4 mm). This means that the specially designed sample is mainly in compression when the deformation is relatively small, while the sample becomes tensile and cracks develop faster as deformation increases.

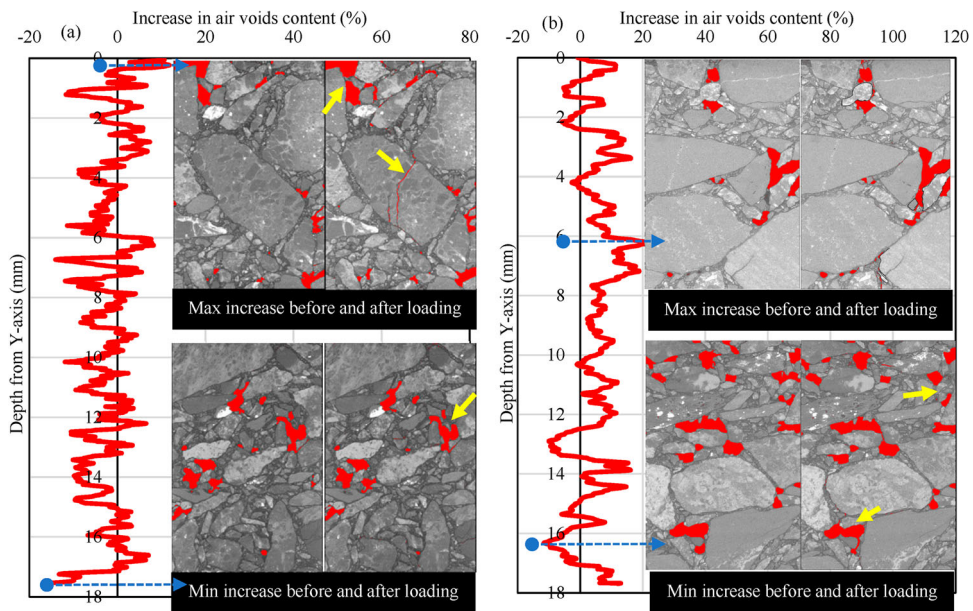


Figure 11. Increase in air voids content at (a) 0.4 and (b) 0.6 mm vertical deformation and the images at the position of the max and min increase in air voids content in Y direction.

To capture crack geometry, images of the slices representing the maximum and minimum increase in the AVC in the Y direction at six different vertical deformations were collected; these are shown in Figures 11–13. It can be seen that air voids are squeezed or stretched, and cracks are observed developing at these positions. Figures 11 and 12 illustrate the images at the position of the minimum increase in the AVC. Air voids can be seen squeezed at these positions and the larger the vertical deformation, the more the air voids are squeezed. Although the samples were compressed at these positions and the dominant damage is in the form of air voids being squeezed, the cracks still developed in accordance with the law found in Section 4.1, which is that microcracks initiate at small deformation (Figure 11), then develop steadily (Figure 12(a,b)) and finally connect together to form macrocracks (Figure 12(c,d)). Figure 13 shows the images at the position of the maximum increase in the AVC. Air voids can be seen stretched at these positions, and the larger the vertical deformation, the more the air voids are stretched. The dominant damage is in the form of cracks when samples were under tensile stress.

To further understand crack initiation and propagation, images at the positions where the maximum increase in the AVC occurred in the X direction were also taken; these are shown in Figures 14 and 15 and were used for comparison to the results in the Y direction. In the X direction (Figure 14) it can be concluded that the change of air voids after loading becomes more obvious with the increase of vertical deformation, and the largest change in the AVC also appears in the middle part of the sample, which agrees with the maximum tension occurring in the middle of the sample.

The impact of the form of the aggregates on fatigue cracking is also explored here. Flat and elongated particles are defined where the dimension ratio (width to thickness or length to width) exceeds 3:1 (Kandhal & Parker, 1998). It has been determined that flat and elongated coarse aggregate particles have some influence on the performance of asphalt mixtures, as such particles tend to break down (Li & Kett, 1967). Asphalt mixtures containing 30% or more flat particles have been shown to have poor properties compared to mixtures with lower percentages of flat particles (Stephens, 1974). In this paper, cracks were found to have initiated and propagated adjacent to flat and elongated aggregates, as shown in Figures 12(d) and 14(b). Cracks were also observed initiating and propagating in interfaces between the mastic and flat and elongated aggregates, as shown in Figures 11(a) and 13(b,d). Air

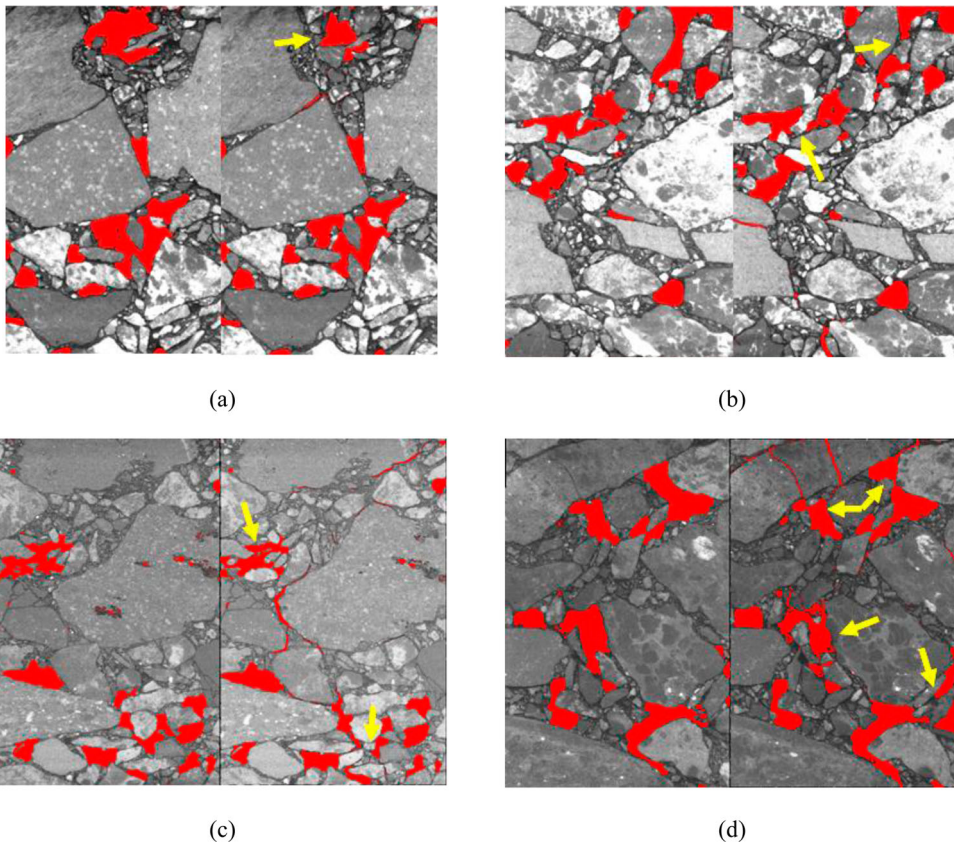


Figure 12. The images at the position of the min increase in air voids content at (a) 0.8, (b) 0.9, (c) 1.1 and (d) 1.4 mm in Y direction.

voids also tend to expand at interfaces between mastic and flat and elongated aggregates, as shown in Figures 13(d) and 14(b).

The irregular shape of aggregates may lead to stress concentrations in asphalt mixtures, consequently causing the initiation and propagation of microcracks, which will finally change the macrostructure and microstructure of the material leading to a deterioration of the mixture's overall strength. Fractured faces, angularity and texture are often described as irregularities with examples of these shown in Figure 16. Angularity describes the edge sharpness of aggregate particles. The larger the angularity of aggregate, the sharper its edges. The texture expresses the relative surface roughness of aggregate particles (Monismith, 1970). The images captured in this paper show that cracks often occurred at interfaces between mastic and non-angular aggregates, as shown in Figures 11(b), 12(c) and 13(b). Cracks were also observed to occur within non-angular aggregates, as shown in Figure 14(a). Reasonable angularity and texture ensure enough interlock friction between aggregates. However, when the angularity continues to increase, cracks tend to initiate and propagate, as shown in Figures 13(a–c) and 15(a,b). Figure 11(a) shows cracks also tend to develop within aggregates with very angular but less textured surfaces. Fatigue cracking behaviour also became more complicated with vertical deformation increase, as shown in Figure 15(c,d). The development of cracks follows the principles described above, but the increased vertical deformation results in coarse aggregates with smooth surfaces moving with the surrounding binder and fine aggregates.

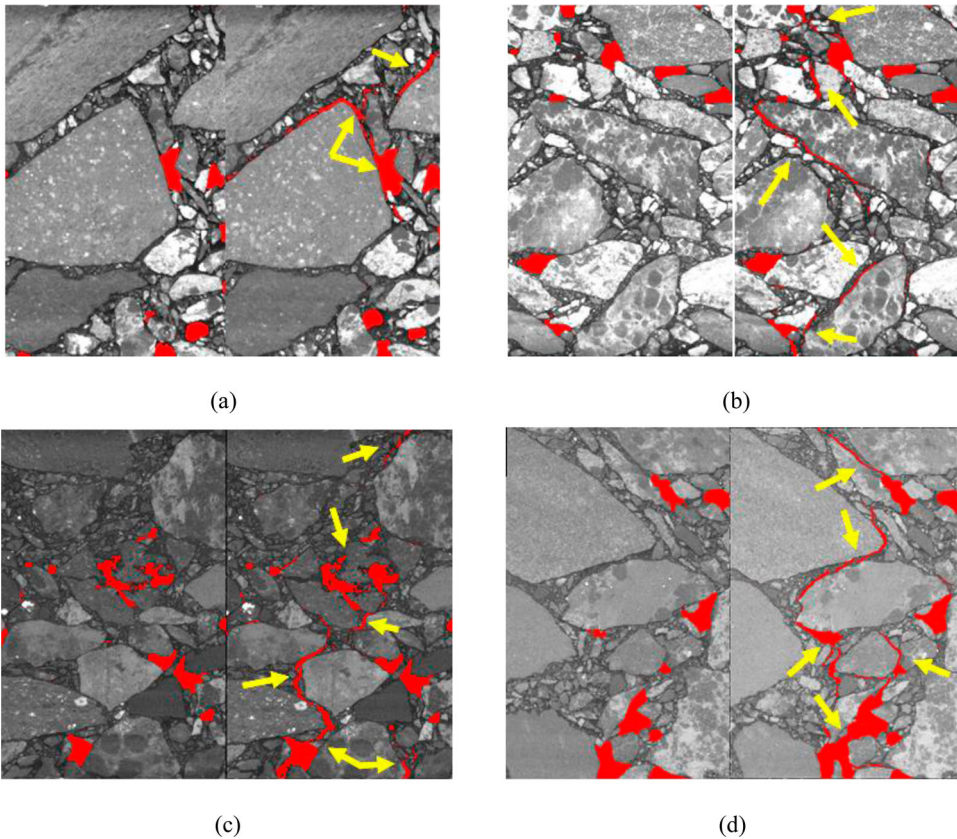


Figure 13. The images at the position of the max increase in air voids content at (a) 0.8, (b) 0.9, (c) 1.1 and (d) 1.4 mm in Y direction.

4.3. Air voids surface area distribution

The air voids surface area (AVSA, mm^2) distribution at 0.4 mm vertical deformation is shown in Figure 17. It can be seen that air voids with a surface area less than 0.3 mm^2 account for the majority of the voids. The number of air voids decreases exponentially when the surface area is larger than 0.3 mm^2 . The number of air voids with a surface area larger than 2.3 mm^2 , which is $1/3$ of the maximum air voids surface area ($\text{MaxAVSA} = 6.9 \text{ mm}^2$), is very small. The AVSAI in three ranges (less than 0.3 , $0.3 \text{ mm}^2 - 1/3$ of MaxAVSA and larger than $1/3$ of MaxAVSA) were calculated, as shown in Figure 18. The AVSAI when the area is less than 0.3 mm^2 is stable and sustained as the vertical deformation increases. There is no obvious AVSAI in the range ($0.3 \text{ mm}^2 - 1/3$ of MaxAVSA). When the area is larger than $1/3$ of MaxAVSA , AVSAI grows rapidly as the vertical deformation is increased. It was found that air voids with large surface areas (macrocracks) are easier to expand and develop when the vertical deformation is large; however, air voids with small surface area (microcracks) continue initiating and propagating no matter whether the deformation is large or small. Previous research has defined the fracture processes, making it easier to understand the damage evolution laws; however, both the visualisation using high-resolution X-ray CT images and the results of AVSA distribution analysis prove that microcracks develop continuously throughout the whole fatigue process.

4.4. Results of volume and surface area parameters

Generally, the volume and surface area of air voids in asphalt concrete can be used to characterise the damage status of asphalt concrete, the higher the volume and surface area of air voids, the more

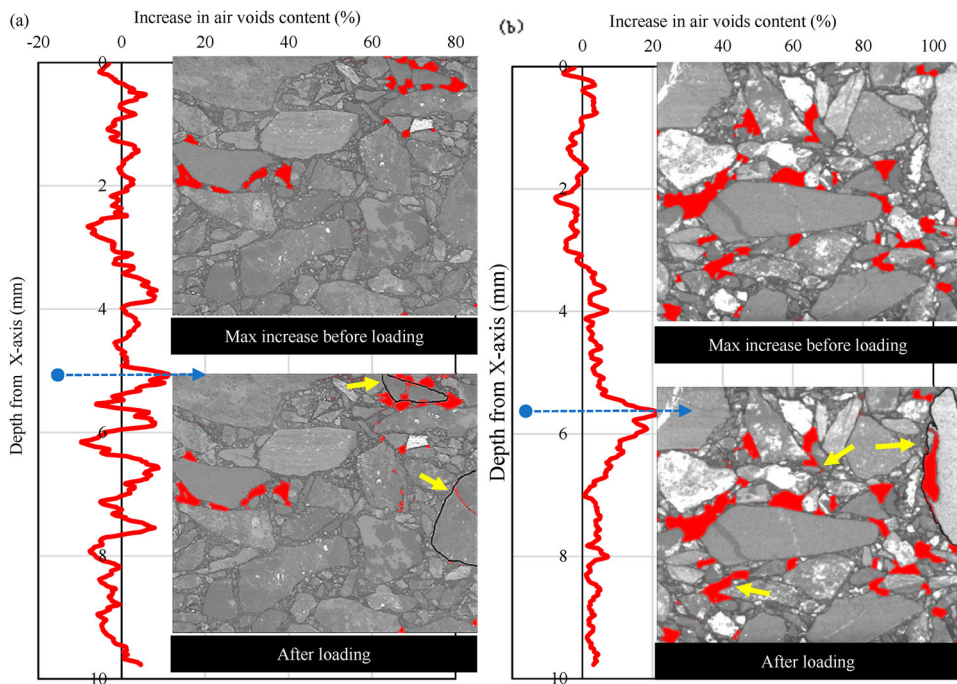


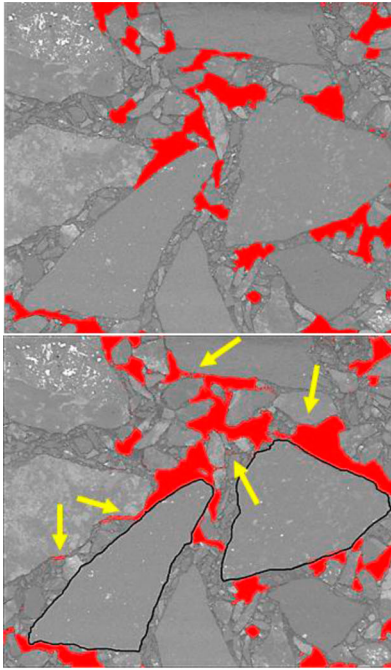
Figure 14. Increase in air voids content at (a) 0.4 and (b) 0.6 mm vertical deformation and the images at the position of the max and min increase in air voids content in X direction.

Table 2. Volume and area parameters of samples.

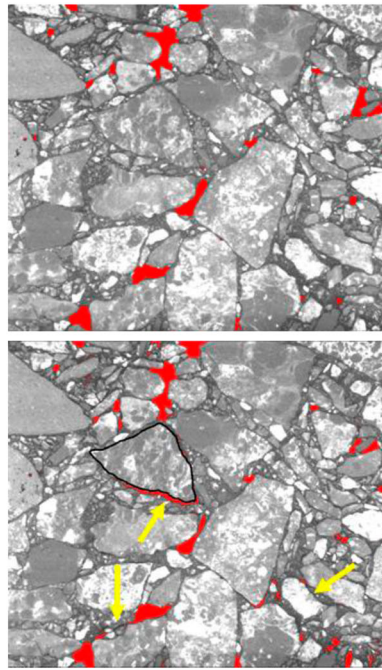
Sample ID	Vertical deformation(mm)	AVC _{pre} (%)	AVC _{after} (%)	AVCC (%)	AVCI (%)	AVSA _{pre} (mm ²)	AVSA _{after} (mm ²)	AVSAC (mm ²)	AVSAI (%)
1	0.4	3.05	3.19	0.14	4.59	1976.63	2022.06	45.43	2.30
2	0.6	5.54	5.90	0.36	6.50	2490.83	3036.81	545.99	21.92
3	0.8	6.55	7.19	0.63	9.77	3744.35	4313.69	569.34	15.21
4	0.9	4.35	5.24	0.89	20.38	2179.39	2950.45	771.06	35.38
5	1.1	3.54	4.56	1.02	28.89	1994.41	3049.32	1054.91	52.89
6	1.4	5.40	6.91	1.51	27.96	2447.90	3676.80	1228.90	50.20

serious the damage is in the asphalt concrete (Song, 2004; Khan & Collop, 2010; Li et al., 2020). The volume and surface area parameters of samples with different vertical deformations are shown in Table 2. It can be seen from Table 2 that the air voids content change (AVCC) becomes more obvious with the increase of vertical deformation (0.14% at 0.4 mm while 1.5% at 1.4 mm), which demonstrates that the damage continues to accumulate. The air voids content basically increases with the increase of vertical deformation from 0.4 to 1.1 mm; however, it slows down when the deformation is higher than 1.1 mm. The reason is that the samples have probably effectively failed at the relatively larger deformations of both 1.1 and 1.4 mm.

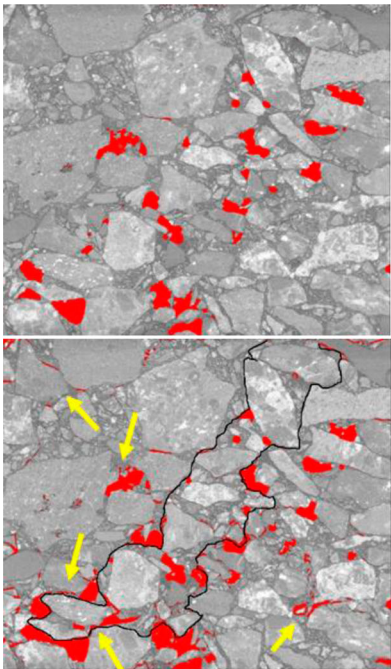
In addition, the same tendency can be found for the air voids surface area change (AVSAC). With increasing vertical deformation, the AVSAC becomes more obvious (45.43 mm² at 0.4 mm while 1228.90 mm² at 1.4 mm). The air voids surface area increase (AVSAI) basically increases with the increase of vertical deformation; however, the change rate increases suddenly at 0.6 mm (21.92%) and decreases after 1.1 mm. This indicates that the cracks develop rapidly at 0.6 mm, and sample failure occurs after the deformation is higher than 1.1 mm.



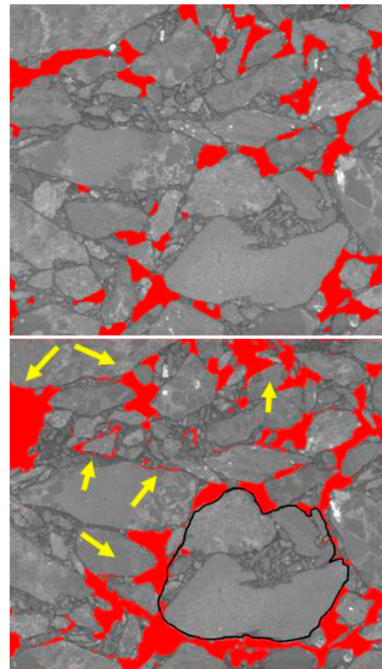
(a)



(b)



(c)



(d)

Figure 15. The images at the position of the max increase in air voids content at (a) 0.8, (b) 0.9, (c) 1.1 and (d) 1.4 mm in X direction.

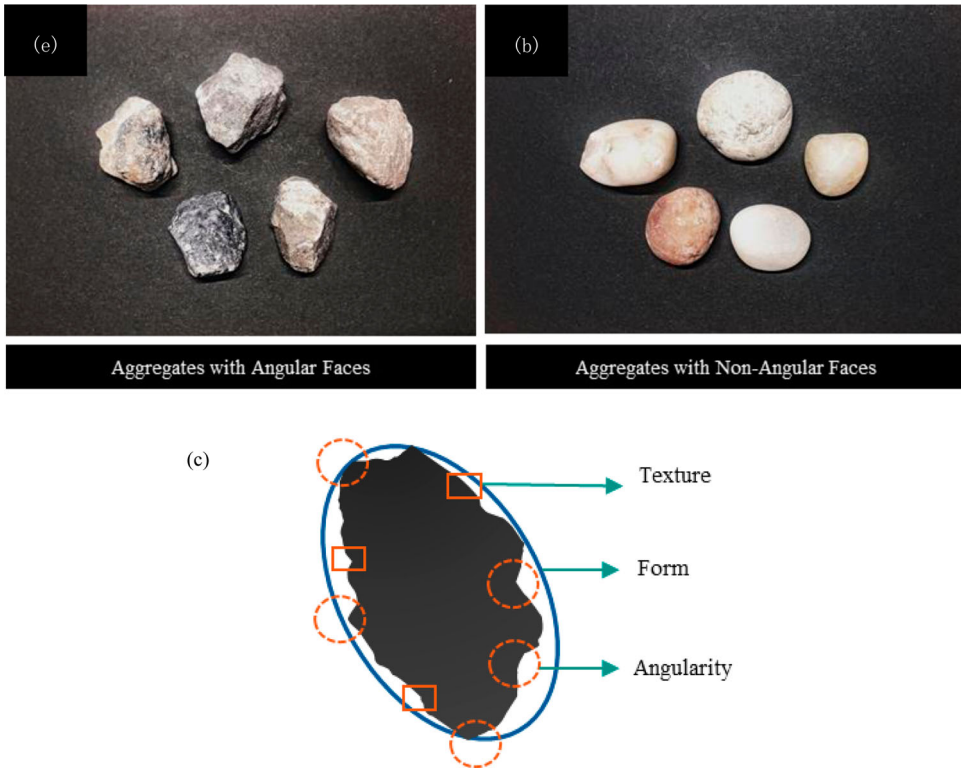


Figure 16. Illustration of morphological characteristic of aggregates: (a) angular and non-angular aggregate; (b) aggregate with many fractured faces; (c) shape characterization (Kandhal & Parker, 1998).

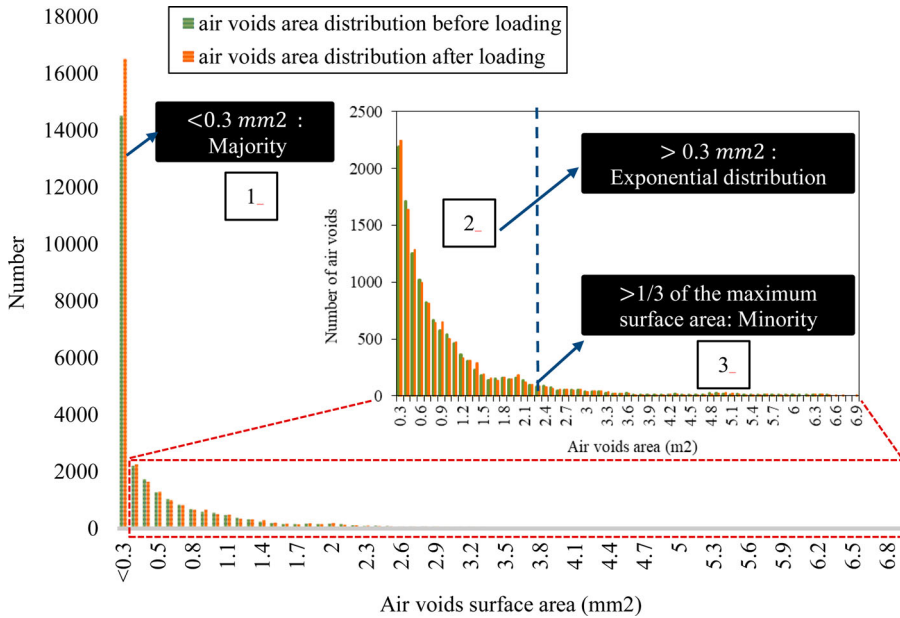


Figure 17. Air voids surface area distribution of the whole sample (at 0.4 mm vertical deformation).

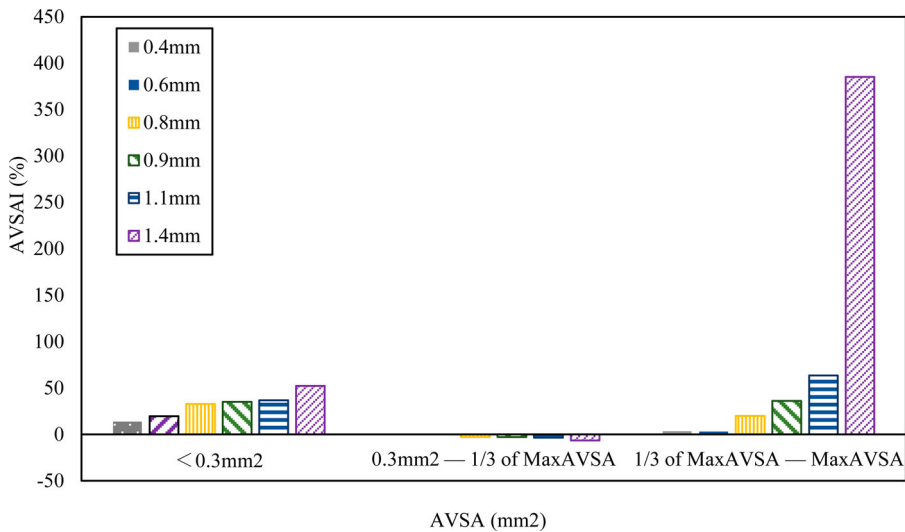


Figure 18. Calculation of AVSAI of three ranges showed in Figure 17.

5. Conclusions

In this paper, high-resolution X-ray CT is used to characterise fatigue damage of asphalt mixtures based on specially designed small samples tested using ITFT. Air voids content and surface area distributions before and after loading were calculated and analysed. The main conclusions of the study are as follows:

1. High-resolution imaging of CT scans of small-size indirect tensile fatigue specimens shows that the main failure mode at 5°C is debonding at the interfaces of aggregates and mastic, which belongs to an adhesive failure mode.
2. The fatigue damage process consists of three distinct stages. At the first stage, deformation develops rapidly before slowing down, only a few microcracks occur at the aggregate–mastic interfaces; at the second stage, the vertical deformation of asphalt concrete develops approximately linearly, the microcracks spread continuously, and some microcracks connect; at in the third stage, the deformation becomes rapid once again, the air voids grow rapidly, and microcracks emerge swiftly.
3. The sample is mainly in compression when the deformation is relatively small. However, it changes to a predominantly tensile strain with the increase of deformation, and cracks develop faster as deformation increases. The maximum increase in the AVC (fatigue damage) often occurs near the middle area of the sample.
4. Both the visualisation based on X-ray CT images and the results of AVSA distribution indicate that the microcracks (characterised as small size air voids) develop continuously throughout the entire fatigue process.
5. The AVCC value becomes more obvious with increasing vertical deformation. The AVCI basically increases with the increase of vertical deformation; however, it slows down when the deformation becomes very large and the reason is that the samples have effectively failed. The same tendency can be found for the AVSAC and AVSAI values with increasing vertical deformation.

Disclosure statement

No potential conflict of interest was reported by the author(s).

ORCID

Anqi Chen  <http://orcid.org/0000-0001-8585-8556>

References

- Aliha, M. R. M., Fazaeli, H., Aghajani, S., & Moghadas Nejad, F. (2015). Effect of temperature and air void on mixed mode fracture toughness of modified asphalt mixtures. *Construction and Building Materials*, *95*, 545–555. <https://doi.org/10.1016/j.conbuildmat.2015.07.165>
- Braz, D., Lopes, R. T., & Da Motta, L. M. G. (1999). Analysis of the percentage voids of test and field specimens using computerized tomography. *Nuclear Instruments and Methods in Physics Research Section A: Accelerators, Spectrometers, Detectors and Associated Equipment*, *422*(1–3), 942–948. [https://doi.org/10.1016/S0168-9002\(98\)01051-1](https://doi.org/10.1016/S0168-9002(98)01051-1)
- British Standards Institution. (2007). Bitumen and bitumen binders, Measurement of density and specific gravity. Capillary-stoppered pyknometer method BS 2000-549, London.
- British Standards Institution. (2015a). Methods of test for petroleum and its products, Bitumen and bituminous binders – determination of needle penetration, BS EN 1426, London.
- British Standards Institution. (2015b). Methods of test for petroleum and its products, bitumen and bituminous binders – determination of the softening point. Ring and Ball method, BS EN 1427, London.
- British Standards Institution. (2016a). Bituminous mixtures – material specifications. Asphalt Concrete, BS EN 13108-1, London.
- British Standards Institution. (2016b). Bituminous mixtures – test methods for hot mix asphalt – Part 35: Laboratory mixing, BS EN 12697-35, London.
- British Standards Institution. (2018a). Bitumen and bituminous binders – determination of dynamic viscosity of bituminous binder using a rotating spindle apparatus, BS EN 13302, London.
- British Standards Institution. (2018b). Bituminous mixtures – test methods – resistance to fatigue, BS EN 12697-24, London.
- British Standards Institution. (2019). Bituminous mixtures – test methods for hot mix asphalt – Part 33: Specimen prepared by roller compactor, BS EN 12697-33, London.
- Castillo, D., Caro, S., Darabi, M., & Masad, E. (2015). Studying the effect of microstructural properties on the mechanical degradation of asphalt mixtures. *Construction and Building Materials*, *93*, 70–83. <https://doi.org/10.1016/j.conbuildmat.2015.05.108>
- Chen, A., Airey, G., Thom, N., Litherland, J., & Nii-Adjei, R. A. (2021). Modelling the stiffness development in asphalt concrete to obtain fatigue failure criteria. *Construction and Building Materials*, *306*, 124837.
- Coleri, E., Harvey, J. T., Yang, K., & Boone, J. M. (2012). A micromechanical approach to investigate asphalt concrete rutting mechanisms. *Construction and Building Materials*, *30*, 36–49. <https://doi.org/10.1016/j.conbuildmat.2011.11.041>
- Coleri, E., Harvey, J. T., Yang, K., & Boone, J. M. (2013). Micromechanical investigation of open-graded asphalt friction courses' rutting mechanisms. *Construction and Building Materials*, *44*, 25–34. <https://doi.org/10.1016/j.conbuildmat.2013.03.027>
- Dai, Q. (2010). Prediction of dynamic modulus and phase angle of stone-based composites using a micromechanical finite-element approach. *Journal of Materials in Civil Engineering*, *22*(6), 618–627. [https://doi.org/10.1061/\(ASCE\)MT.1943-5533.0000062](https://doi.org/10.1061/(ASCE)MT.1943-5533.0000062)
- Dowling, N. E. J. A. S. (1976). *Fatigue crack growth during gross plasticity and the J-integral*, 590.
- Eriksen, K. (1993). Microscopical analysis of asphalt-aggregate mixtures related to pavement performance.
- Jacobs, M., Hopman, P., & Molenaar, A. (1996). Application of fracture mechanics principles to analyze cracking in asphalt concrete. *Journal of the Association of Asphalt Paving Technologists*, *65*, 1–39.
- Kandhal, P. S., & Parker, F. (1998). *Aggregate tests related to asphalt concrete performance in pavements* (Vol. 405). Transportation Research Board.
- Khan, R. (2010). *Quantification of microstructural damage in asphalt*. University of Nottingham.
- Khan, R., & Collop, A. C. (2010). The use of X-ray computed tomography to characterize microdamage in asphalt. *Road Materials and Pavement Design*, *11*(Suppl 1), 89–109. <https://doi.org/10.1080/14680629.2010.9690328>
- Khosravi, H., Abtahi S, M., Koosha, B., & Manian, M. (2013). An analytical-empirical investigation of the bleeding mechanism of asphalt mixes. *Construction and Building Materials*, *45*, 138–144. <https://doi.org/10.1016/j.conbuildmat.2013.04.004>
- Kim, Y. R., Aragao, F. T. S., Allen, D. H., Aragão, F. T. S., & Little, D. N. (2010). Damage modeling of bituminous mixtures considering mixture microstructure, viscoelasticity, and cohesive zone fracture. *Canadian Journal of Civil Engineering*, *37*(8), 1125–1136. <https://doi.org/10.1139/L10-043>
- Kodippily, S., Henning, T. F. P., Ingham J, M., & Holleran, G. (2014). Computed tomography scanning for quantifying chipseal material volumetrics. *Journal of Computing in Civil Engineering*, *28*(3), 04014002. [https://doi.org/10.1061/\(ASCE\)CP.1943-5487.0000284](https://doi.org/10.1061/(ASCE)CP.1943-5487.0000284)
- Kutay, M. E., Arambula, E., Gibson, N., & Youtcheff, J. (2010). Three-dimensional image processing methods to identify and characterise aggregates in compacted asphalt mixtures. *International Journal of Pavement Engineering*, *11*(6), 511–528. <https://doi.org/10.1080/10298431003749725>

- Li, M. C., & Kett, I. (1967). *Influence of coarse aggregate shape on the strength of asphalt concrete mixtures*. Highway Research Record (178).
- Li, Y., Wu, S., Dai, Y., Li, C., Song, W., Li, H., Li, C., & Shu, B. (2020). Transitions of component, physical, rheological and self-healing properties of petroleum bitumen from the loose bituminous mixture after UV irradiation. *Fuel*, 262, 116507.
- Liu, P., Hu, J., Wang, D., Oeser, M., Alber, S., Ressel, W., & Canon Falla, G. (2017). Modelling and evaluation of aggregate morphology on asphalt compression behavior. *Construction and Building Materials*, 133, 196–208. <https://doi.org/10.1016/j.conbuildmat.2016.12.041>
- Maggiore, C., & Airey, G. (2014). *A comparison of different test and analysis methods for asphalt fatigue*. University of Nottingham.
- Majidzadeh, K., Kauffmann, E., & Ramsamooj, D. (1971). *Application of fracture mechanics in the analysis of pavement fatigue*. Association of Asphalt Paving Technologists Proc.
- Masad, E., Jandhyala, V. K., Dasgupta, N., Somadevan, N., & Shashidhar, N. (2002). Characterization of air void distribution in asphalt mixes using X-ray computed tomography. *Journal of Materials in Civil Engineering*, 14(2), 122–129. [https://doi.org/10.1061/\(ASCE\)0899-1561\(2002\)14:2\(122\)](https://doi.org/10.1061/(ASCE)0899-1561(2002)14:2(122))
- Masad, E., Muhunthan, B., Shashidhar, N., & Harman, T. (1999). Internal structure characterization of asphalt concrete using image analysis. *Journal of Computing in Civil Engineering*, 13(2), 88–95. [https://doi.org/10.1061/\(ASCE\)0887-3801\(1999\)13:2\(88\)](https://doi.org/10.1061/(ASCE)0887-3801(1999)13:2(88))
- Miljković, M., & Radenberg, M. (2014). Effect of compaction energy on physical and mechanical performance of bitumen emulsion mortar. *Materials and Structures*, 49, <https://doi.org/10.1617/s11527-014-0488-z>
- Mohajeri, M., Molenaar, A. A. A., & Van de Ven, M. F. C. (2014). Experimental study into the fundamental understanding of blending between reclaimed asphalt binder and virgin bitumen using nanoindentation and nano-computed tomography. *Road Materials and Pavement Design*, 15(2), 372–384. <https://doi.org/10.1080/14680629.2014.883322>
- Monismith, C. L. (1970). *Influence of shape, size, and surface texture on the stiffness and fatigue response of asphalt mixtures*. Highway Research Board Special Report, (109).
- Monismith, C. L. (1992). Analytically based asphalt pavement design and rehabilitation: Theory to practice, 1962–1992.
- Paris, P. (1963). A critical analysis of crack propagation laws. *Journal of Basic Engineering*, 85, 528–534.
- Rami, K. Z., Amelian, S., Kim, Y. R., You, T., & Little, D. N. (2017). Modeling the 3D fracture-associated behavior of viscoelastic asphalt mixtures using 2D microstructures. *Engineering Fracture Mechanics*, 182, 86–99. <https://doi.org/10.1016/j.engfracmech.2017.07.015>
- Read, J. M., Brown, S. F., & Pell, P. S. (1996). *Fatigue cracking of bituminous paving mixtures*. University of Nottingham.
- Seo, Y., & Kim, Y. R. (2008). Using acoustic emission to monitor fatigue damage and healing in asphalt concrete. *KSCCE Journal of Civil Engineering*, 12(4), 237–243. <https://doi.org/10.1007/s12205-008-0237-3>
- Song, I. (2004). *Damage analysis in asphalt concrete mixtures based on parameter relationships*. Texas A&M University.
- Stephens, J. E. (1974). *Effect of aggregate shape on bituminous mix character* (No. JHR 74-87 Final Rpt.).
- Sulaiman, S., & Stock, A. (1995). The use of fracture mechanics for the evaluation of asphalt mixes. *Journal of the Association of Asphalt Paving Technologists*, 64, 500–533.
- Tashman, L., Masad, E., Little, D., & Lytton, R. L. (2004). Damage evolution in triaxial compression tests of HMA at high temperatures. *Journal of the Association of Asphalt Paving Technologists*, 73, 53–87.
- Tashman, L., Masad, E., Little, D., & Zbib, H. (2005). A microstructure-based viscoplastic model for asphalt concrete. *International Journal of Plasticity*, 21(9), 1659–1685. <https://doi.org/10.1016/j.ijplas.2004.11.008>
- Tashman, L. S., Masad, E., Peterson, B., & Saleh, H. (2000). *Internal structure analysis of asphalt mixes to improve the simulation of superpave gyratory compaction to field conditions*. Washington State University.
- Trawiński, W., Tejchman, J., & Bobiński, J. (2018). A three-dimensional meso-scale modelling of concrete fracture, based on cohesive elements and X-ray μ CT images. *Engineering Fracture Mechanics*, 189, 27–50. <https://doi.org/10.1016/j.engfracmech.2017.10.003>
- Wang, L., Paul, H. S., Harman, T., & D'Angelo, J. (2004). Characterization of aggregates and asphalt concrete using X-Ray computerized tomography-A state of the art report. *Journal of the Association of Asphalt Paving Technologists*, 73, 467–500. <https://doi.org/10.1677/joe.0.1540103>
- Yin, A., Yang, X., Zhang, C., Zeng, G., & Yang, Z. (2015). Three-dimensional heterogeneous fracture simulation of asphalt mixture under uniaxial tension with cohesive crack model. *Construction and Building Materials*, 76, 103–117. <https://doi.org/10.1016/j.conbuildmat.2014.11.065>
- Yue, Z. Q., Bekking, W., & Morin, I. (1995). Application of digital image processing to quantitative study of asphalt concrete microstructure. *Transportation Research Record*, 1492, 53–60.
- Zeilew, H. M., & Papagiannakis, A. T. (2011). A volumetrics thresholding algorithm for processing asphalt concrete X-ray CT images. *International Journal of Pavement Engineering*, 12(6), 543–551. <https://doi.org/10.1080/10298436.2011.561345>
- Zhang, B., Wang, L., & Tumay, M. T. (2006). *An evaluation of the stress non-uniformity due to the heterogeneity of AC in the indirect tensile test/asphalt concrete: Simulation, modeling, and experimental characterization*, 29–43.